

High-Performance Flexible Self-Powered Photodetectors Utilizing Spontaneous Electron and Hole Separation in Quasi-2D Halide Perovskites

Zhengxun Lai, You Meng, Qi Zhu, Fei Wang, Xiuming Bu, Fangzhou Li, Wei Wang, Chuntai Liu, Feng Wang, and Johnny C. Ho*

Although there are recent advances in many areas of quasi-2D halide perovskites, photodetectors based on these materials still cannot achieve satisfactory performance for practical applications where high responsivity, fast response, self-powered nature, and excellent mechanical flexibility are urgently desired. Herein, utilizing one-step spin-coating method, self-assemble quasi-2D perovskite films with graded phase distribution in the order of increasing number of metal halide octahedral layers are successfully prepared. Gradient type-II band alignments along the out-of-plane direction of perovskites with spontaneous separation of photo-generated electrons and holes are obtained and then employed to construct self-powered vertical-structure photodetectors for the first time. Without any driving voltage, the device exhibits impressive performance with the responsivity up to 444 mA W^{-1} and ultrashort response time down to $52 \mu\text{s}$. With a bias voltage of 1.5 V , the device responsivity becomes 3463 mA W^{-1} with the response speed as fast as $24 \mu\text{s}$. Importantly, the device's mechanical flexibility is greatly enhanced since the photocurrent prefers flowing through the metal halide octahedral layers between the top and bottom contact electrodes in the vertical device structure, being more tolerant to film damage. These results evidently indicate the potential of graded quasi-2D perovskite phases for next-generation optoelectronic devices.

1. Introduction

In recent years, photodetectors have become more and more important for many technological applications, such as biological imaging, optical communication, and surveillance.^[1–3] They


all require high-performance photodetectors with great responsivity, fast response speed, good mechanical flexibility, and even self-powered nature. In this regard, there is always a search for suitable active device materials as well as appropriate device structures to achieve the required performance parameters of photodetectors. Among many recent developments, organic–inorganic halide perovskites, such as methylammonium lead halides, MAPbX_3 ($X = \text{I, Br, and Cl}$), have been widely demonstrated as promising active materials for photodetectors due to their excellent optoelectronic properties.^[4–9] However, these perovskite materials have a major drawback of poor ambient stability, which greatly hampers their utilization for photodetectors and other optoelectronics devices.^[10,11]

In order to tackle this stability issue, quasi-2D perovskites are newly proposed, where the bulky organic molecules, including $\text{CH}_3(\text{CH}_2)_3\text{NH}_3^+$ (butylamine, BA) or $\text{C}_6\text{H}_5(\text{CH}_2)_2\text{NH}_3^+$ (phenethylammonium, PEA), are

inserted into the conventional 3D halide perovskite lattice (e.g., MAPbI_3) to severe as the spacer cation.^[12–14] This kind of quasi-2D halide perovskites, also known as Ruddlesden–Popper perovskites (RPPs), can exhibit relatively high ambient stability over 3D perovskites because of their

Z. X. Lai, Y. Meng, Q. Zhu, Dr. F. Wang, Dr. X. M. Bu, Dr. F. Z. Li, W. Wang, Prof. F. Wang, Prof. J. C. Ho
Department of Materials Science and Engineering
City University of Hong Kong
Kowloon 999077, Hong Kong SAR
E-mail: johnnyho@cityu.edu.hk

Dr. F. Wang
State Key Laboratory of Luminescence and Applications
Changchun Institute of Optics
Fine Mechanics and Physics
Chinese Academy of Sciences
Changchun 130021, China

 The ORCID identification number(s) for the author(s) of this article can be found under <https://doi.org/10.1002/smll.202100442>.

Dr. F. Wang, W. Wang, Prof. J. C. Ho
State Key Laboratory of Terahertz and Millimeter Waves
City University of Hong Kong
Kowloon 999077, Hong Kong SAR

Prof. C. T. Liu
Key Laboratory of Advanced Materials Processing and Mold
(Zhengzhou University)
Ministry of Education
Zhengzhou 450002, China

Prof. J. C. Ho
Institute for Materials Chemistry and Engineering
Kyushu University
Fukuoka 816–8580, Japan

DOI: 10.1002/smll.202100442

hydrophobic nature of the spacer molecules.^[15] RPPs can be described with the general chemical formula as $L_2A_{n-1}B_nX_{3n+1}$, in which L represents the large-scale organic spacer cation, A and B denote the regular cations, and X refers to the halide constituent (for their 3D counterpart, A and B are located at the corner and body center of the crystal cell and X is located at the face center, respectively).^[16,17] In other words, the $A_{n-1}B_nX_{3n+1}$ unit is sandwiched between two L cation layers, where the variable n is an integer, representing the number of metal halide octahedral layers that get sandwiched there.

Although the ambient stability of RPPs is superior to their 3D counterparts, their photoelectric performance is still not satisfactory for practical applications.^[18] Moreover, the mechanical flexibility of RPPs is relatively poor owing to the weak van der Waals interaction between the two spacer cations, hindering their use for flexible devices.^[19–21] Meanwhile, self-powered photodetectors with high performance are also highly preferred since they can operate without connecting to any external energy sources.^[22,23] In specific, the structure of self-powered photodetectors usually contains several essential layers, such as the electron transport layer, active layer, and hole transport layer, etc.^[24–26] Although this configuration can endow self-powered photodetectors with satisfactory performance, there are still substantial weaknesses. First, the fabrication process of these different layers is quite complex and often makes the layers interpenetrate and even denature each other, restricting the application of fabricated devices.^[27] Besides, the commonly used electron transport layers, such as TiO_2 , need to be annealed at a relatively high temperature over 400 °C, which is incompatible with most device substrates of flexible photodetectors.^[28,29] In addition, the high-performance organic materials based hole transport layer, including spiro-MeOTAD, PTAA, and PEDOT:PSS, are not only deliquescent but also expensive, which are not the appropriate device materials for large-scale fabrication.^[30,31] As a result, there is an urgent need to break this bottleneck to achieve a cost-effective scheme to construct the highly-efficient flexible self-powered photodetectors with a simple device configuration.

Lately, various arrangements of graded RPP phases (with the changing n values) capable to establish tunable band alignment and associated energy cascade transfer processes have also been proposed and widely studied for different utilization scenarios.^[32–38] Herein, utilizing this unique nature of RPPs, high-quality RPP films composed of the relatively short-chain iBA as spacer cations ($iBA_2(MA)_{n-1}Pb_nI_{3n+1}$) with gradient band alignments are successfully synthesized by a simple one-step spin-coating process. It is observed that the graded RPP phases distribute sequentially with the increasing n values towards the film surface. This way, by constructing the proper bottom and top contact electrodes, vertical-structure photodetectors based on the graded RPP phases can be readily achieved. Importantly, these photodetectors exhibit self-powered characteristics with superior performance. Under 450 nm irradiation, the responsivity is as high as 444 mA W⁻¹ and the rise and decay times can be down to 52 and 63 μs, respectively. When a bias voltage of 1.5 V is applied, the highest responsivity can arrive at 3463 mA W⁻¹ with the rise and decay times as short as 24 and 25 μs, accordingly. This kind of RPPs based photodetectors are capable to deliver excellent mechanical flexibility because of their vertical

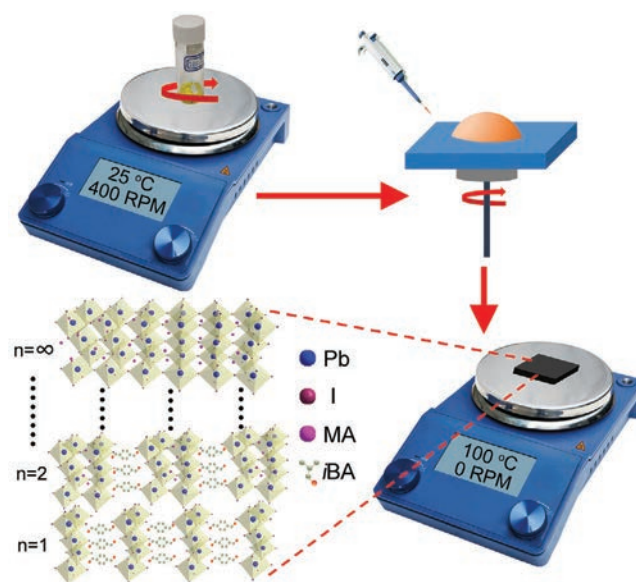


Figure 1. Schematic illustration of the fabrication process of RPP films.

device structure, which is meaningful to overcome the poor flexibility of RPPs. All these results would pave a promising way to break the bottleneck of self-powered flexible photodetectors based on appropriate designs of the RPPs.

2. Results and Discussion

Figure 1 illustrates the fabrication process of the RPP films. In particular, the films are designed to have the graded RPP phases naturally aligned along the out-of-plane direction with increasing n values towards the film surface. The fabrication details will be demonstrated hereinafter. In order to characterize the prepared films, the corresponding X-ray diffraction (XRD) patterns are depicted in Figure S1, Supporting Information. The labels of $n1$, $n2$, $n3$, $n4$, $n5$, $n10$, $n20$, and 3D ($n = \infty$) are used to indicate the samples prepared with different stoichiometric ratios (different n values), distinguishing themselves among different phases (i.e., the $n = 1$, $n = 2$, etc.). The Le Bail refinement of XRD patterns is performed for the $n1$, $n2$, and $n3$ films as shown in Figures S2–S4, Supporting Information. The XRD peaks of different phases are then marked with different specific colors based on the refinement results (Figure S1, Supporting Information). For the sample of $n1$, a series of (001) diffraction peaks are observed, indicating the 2D layered nature stacked along [001] direction of the perovskite film. For the samples of $n2$ and $n3$, besides their typical peaks of (110) and (220), there are additional peaks associated with the $n = 1$, $n = 2$, or $n = 3$ phase, suggesting their mixed-phases nature. For the films of $n4$, $n5$, $n10$, $n20$, and 3D, there are obvious peaks of the (110) and (220) planes, revealing the orientation of these different phases mainly aligned along the [110] direction. It is worth mentioning that since the (110) and (220) peaks of all these phases with different n values are almost located at the same peak location, the exact phases existing in the samples cannot be determined exclusively by identify their XRD patterns.^[18]

In this case, as shown in **Figure 2a**, the absorption spectra for all the samples are measured to further determine their

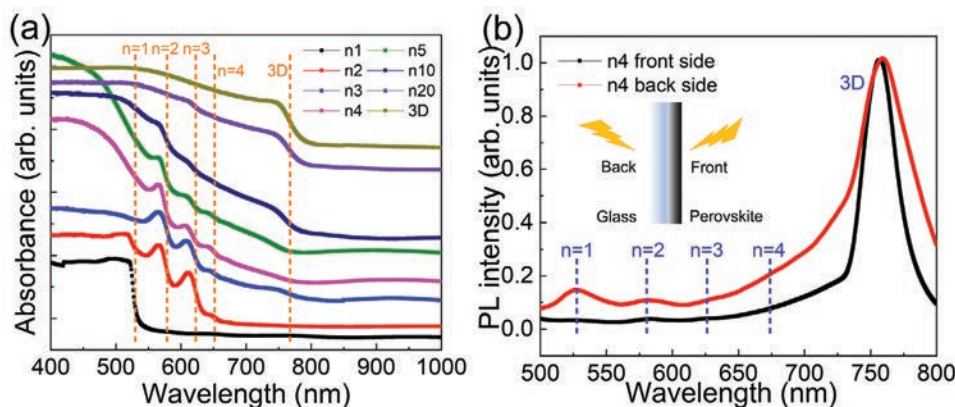


Figure 2. a) Absorption spectra of the prepared films with different n values. b) PL spectra of the n_4 film illuminated from both front and back sides.

composition. The absorption edges of different phases are labeled with the orange dashed lines. It is seen that all these samples, except n_1 and 3D, contain absorption edges of the phases $n = 1, 2, 3, 4$, and ∞ , confirming the mixed-phases nature of prepared films. To thoroughly investigate how these phases distribute within the films, the photoluminescence (PL) spectra of the n_4 sample are measured with both front and back illuminations. For the spectrum under front illumination, the laser with the wavelength of 470 nm is illuminated directly onto the RPP film. For the spectrum under back illumination, the laser is irradiated onto the sample through the glass substrate as illustrated in the inset of Figure 2b. The emission peaks of different phases are labeled with the blue dashed lines. Obviously, there is a dominant emission peak located at 757 nm on both illuminations of the sample, attributable to the phase $n = \infty$. The peaks of $n = 1, 2, 3$, and 4 are observed under the back illumination with decreasing intensity, while there are not such peaks witnessed under the front illumination. This observation suggests that the low n -valued phases prefer to exist at the bottom side of the film, which implies the formation of graded RPP phases here with increasing n values towards the film surface. The front and back side PL spectra of other samples are also measured and presented in Figure S5, Supporting Information. One can see that the PL spectra of n_5 and n_{10} samples are close to that of the n_4 sample. For the films of n_1 and 3D, there is only one single peak positioned at 531 ($n = 1$) and 757 nm (3D), respectively, revealing the pure phase of $n = 1$ and 3D existed in the samples. For the sample of n_{20} , there are also hardly any other peaks observed, except the one at 757 nm, which is caused by the small amount of the spacer cation of *i*BA in the film. However, for the samples of n_2 and n_3 , there are peaks of different phases in both front and back side PL spectra, indicating a large amount of *i*BA can penetrate to the surface of the RPP film. All these PL results demonstrate that an appropriate amount of the spacer cation is necessary to get the desired grading distribution of RPP phases in the films. This feature of the RPP films can be ascribed to the different nucleation order of different phases. It was detected that during the formation of RPP films, the 3D-like phase would first nucleate at the air/liquid interface and then the 2D phases form after that. The order of the nucleation of different phases is crucial to the formation of graded phase distribution.^[34]

At the same time, the morphology of prepared RPP films is evaluated by scanning electron microscopy (SEM) and atomic force microscopy (AFM), as shown in Figures S6 and S7,

Supporting Information. It is clear that the n_{20} and 3D films contain large rod-like grains. As the ratio of the spacer cation of *i*BA increases (i.e., n value decreases), the films become more uniform and smoother. The average surface roughness (R_a) of prepared films is also presented in Figure S7, Supporting Information. Accordingly, the R_a of n_{20} and 3D samples are determined to be 66.2 and 54.1 nm, which are much larger than those of the other films (<11 nm), confirming the better conformality of the low n -valued films. The better quality of the low n -valued films can be attributed to the similar mechanism of the phase segregation demonstrated above. During the spin-coating process, the 3D phase would first nucleate at the surface. For the films with a lower concentration of *i*BA, a large amount of 3D phase gets nucleated at the same time, which makes the surface relatively rough. However, for those films with a relatively higher concentration of *i*BA, the 3D phase nucleates first, and then the other lower n phases nucleate gradually, which is not as hasty as the nucleation of the lower concentration ones. As a result, the films become more conformal with the smoother surface. In particular, the thickness of the n_4 film, the focus of the studied films, is found to be 568 nm based on the cross-section SEM image as shown in Figure S8, Supporting Information.

Taking advantage of these graded RPP phases with increasing n values aligning in the out-of-plane direction towards the film surface, a simple vertical-structure photodetector is designed and fabricated utilizing these prepared films as the active device channels (Figure 4b inset). Since the top contact electrode is employed in this device structure, it is important to first accurately assess the illumination light intensity that can penetrate through the electrode reaching the RRP materials for photo-detection. The optical transmission of the top Au electrode is then measured and presented in Figure S9, Supporting Information. The photodetector based on the n_4 sample is first studied under laser illumination with different wavelengths. Figure 3a shows the current-voltage (I - V) curves of the photodetector with and without the illumination of a 450-nm laser. The I - V curves do not pass through the zero point, revealing the ability for self-powered photodetection of the device. This observation can be ascribed to the particularly graded RPP phase distribution across the film, resulting in a type-II band alignment along the direction perpendicular to the substrate with spontaneous separation of photo-generated electrons and holes (see Figure 3f).

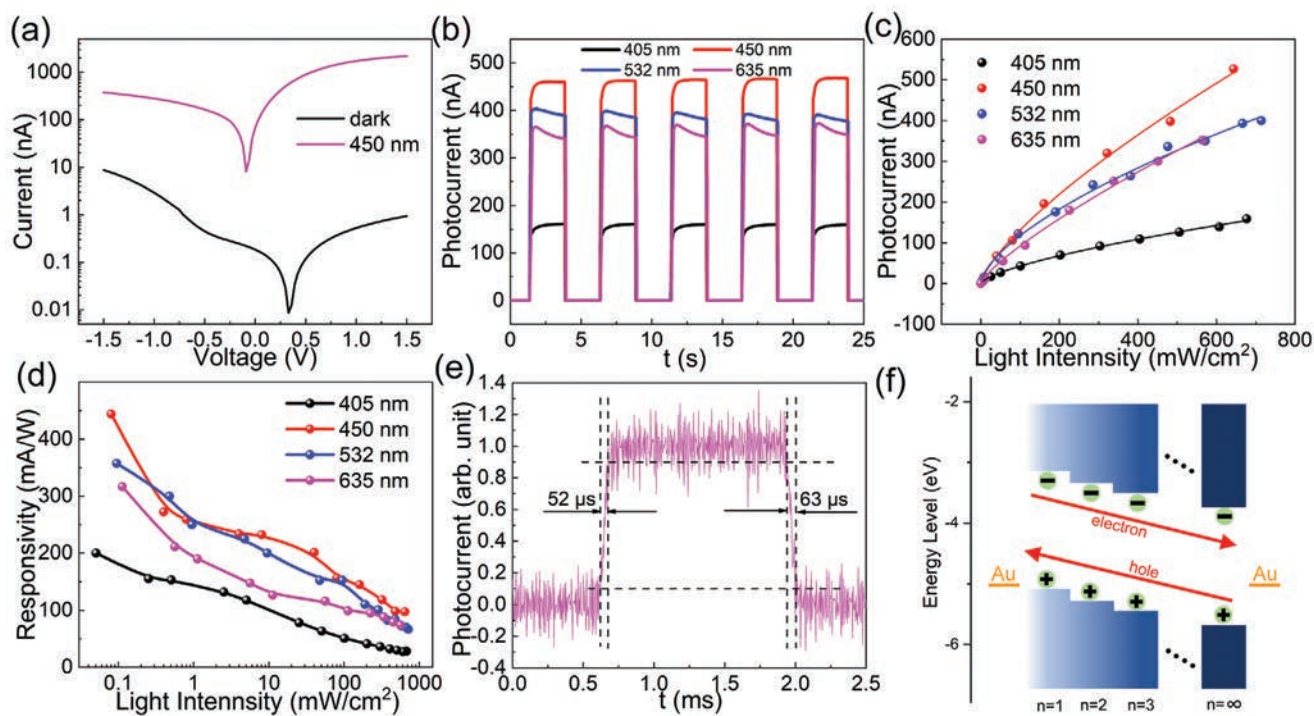


Figure 3. The performance of the self-powered photodetector based on the n4 film as the active layer, where lasers with different wavelengths are applied. a) The I - V curves under dark and 405 nm laser, where the light intensity is set at 950 mW cm^{-2} . b) Time-dependent photoresponse with the light intensity of 560 mW cm^{-2} . c) Dependence of photocurrent on the light intensity. d) Dependence of the responsivity on light intensity. e) High-resolution current versus time curve of the device. f) Energy band diagram of the vertical-structure device.

Under zero bias, an internal electric potential from the low n phases to the high n phases can also exist due to the gradient energy levels. When illumination is introduced, the electron-hole pairs generated in the perovskite layer will separate rapidly under the built-in electric potential. The electrons will transport to the large n side while the holes will move toward the low n side. This way, the device can be operated without applying any bias voltage. Figure 3b shows the on/off switching cycles of the device under different light intensity with a voltage of 0 V, which suggests the good repeatability and stability of the photodetector under monochromatic lights. The maximum on/off current ratio can arrive at 4.2×10^4 . Figure 3c compiles the obtained photocurrents of this self-powered photodetector under different light intensity. The photocurrents exhibit a sub-linear relationship with the light intensity, which can be well fitted by the analytical expression:

$$I_p = A\Phi^\beta \quad (1)$$

where I_p is the photocurrent, A , and β are the fitting parameters, and Φ is the light intensity. The values of β are determined to be 0.67, 0.74, 0.64, and 0.78 from the fitting of the measured data under the illumination of 405, 450, 532, and 635 nm laser, respectively, confirming the sublinear relationship between I_p and Φ . Actually, this sublinear relationship is often observed in layered-material-based photodetectors, which is usually resulted from the complex processes of electron-hole generation, trapping and recombination existed within the films.^[39–41] On the other hand, responsivity (R) is a significant parameter used to

characterize the photodetector performance. R can be defined as the following:

$$R = \frac{I_p}{\Phi S} \quad (2)$$

where S is the active area of the photodetector. Then, Figure 3d depicts the corresponding responsivity values of the device under different excitation wavelengths and intensity. The maximum R is found to be 444 mA W^{-1} , which is comparable or even higher than those of other RPP based photodetectors powered by external bias voltages.^[42] Besides, the detectivity (D) and external quantum efficiency (EQE) of the device are also calculated and shown in Figure S10, Supporting Information, according to the equations of $D = RS^{1/2}/(2eI_{\text{dark}})^{1/2}$ and $\text{EQE} = hcR/e\lambda$, where e , I_{dark} , h , c , and λ represent the electronic charge, dark current of the photodetector, Planck's constant, velocity and wavelength of the incident light, respectively.^[43,44] The largest D and EQE of these self-powered photodetectors are up to 4.1×10^{12} Jones and 122%, accordingly. Moreover, the response speed is another essential performance parameter for photodetectors. As given in the high-resolution photocurrent-time (I_p - t) curve in Figure 3e, the rise (decay) time of the photocurrent is defined as the time interval for the current increasing from 10% to 90% (decreasing from 90% to 10%) of the peak value. The corresponding rise and decay times are found as short as 52 and 63 μs , where these extremely fast response speeds are mostly benefited from the rapid electron and hole separation in the RPP film with the graded phases. Apart from

the self-powered mode, the device operation powered with an external bias voltage of 1.5 V is also carefully investigated. As shown in Figure S11a, Supporting Information, the on/off switching characteristics indicate the excellent reproducibility and stability of the device under different illumination wavelengths, with the maximum on/off current ratio up to 1.5×10^3 . Figure S11b, Supporting Information, displays the photocurrents measured under different light intensities, where a sub-linear relationship is again acquired similar to the one obtained in the self-powered operation. The corresponding responsivity values under different excitation wavelengths and intensities are then calculated (Figure S11c, Supporting Information). The maximum R arrives at 3463 mA W^{-1} , which is much larger than most of the state-of-the-art RPP films based photodetectors, even higher than the single crystal devices.^[42,45–53] Furthermore, the ultra-fast response speed down to $24 \mu\text{s}$ is obtained, being over several orders of magnitude faster than most of the RPP based photodetectors reported ever.^[42,45–53] All these findings demonstrate the superior device performance achieved in the vertical-structure photodetector based on graded RRP phases.

Meanwhile, to shed light on the influence of the spacer cation's (i.e., $i\text{BA}$) concentration on the performance of fabricated photodetectors, all the other RPP films with different n values are also configured into the vertical-structure devices. The dark I - V curves of these devices are first illustrated in Figure S12, Supporting Information. For the samples of $n1$ and 3D, the I - V curves are close to linear, suggesting a nearly ohmic-like contact property between the films and the Au electrodes. However, for

the films of $n2$, $n3$, $n4$, $n5$, $n10$, and $n20$, the I - V curves show an obvious rectification behavior, confirming the existence of an internal self-driven voltage induced by the graded RPP phases. The performance of all different photodetectors was then studied in detail. Figure 4a presents the on/off switching characteristics of devices under a 450-nm laser with a light intensity of 900 mW cm^{-2} and with a bias voltage of 0 V. The excellent reproducibility behavior suggests good reversibility and stability of the photodetectors. Their normalized photocurrents are next plotted with the different concentrations of $i\text{BA}$ in Figure 4b (i.e., different n value). Evidently, when the n value of the RPP films increases, the photocurrent would increase first and then decreases, indicating that a moderate amount of $i\text{BA}$ is necessary to get the proper distribution of graded RPP phases favorable for the photocarrier separation and collection. From the UV-vis absorbance spectra in Figure 2a, we can see, for $n4$, $n5$, $n10$, $n20$, and 3D films, the absorbance peaks of the different phases ($n = 1, 2, 3, 4$) become weaker gradually; hence, the gradient of the phases will become more distinctive as the n value decreases. For $n2$ and $n3$ films, the PL spectra in Figure S5, Supporting Information show that the distribution of the different phases is not very ordered (both the PL spectra from the front and the back sides contain the composition of the low n phases); thus, the type-II band alignment can hardly exist here. As a result, the $n4$ film is believed to have the highest photocurrent and responsibility. Figure 4c demonstrates their photocurrents operated under the self-powered mode with different light intensities. As the n value increases, the changes of

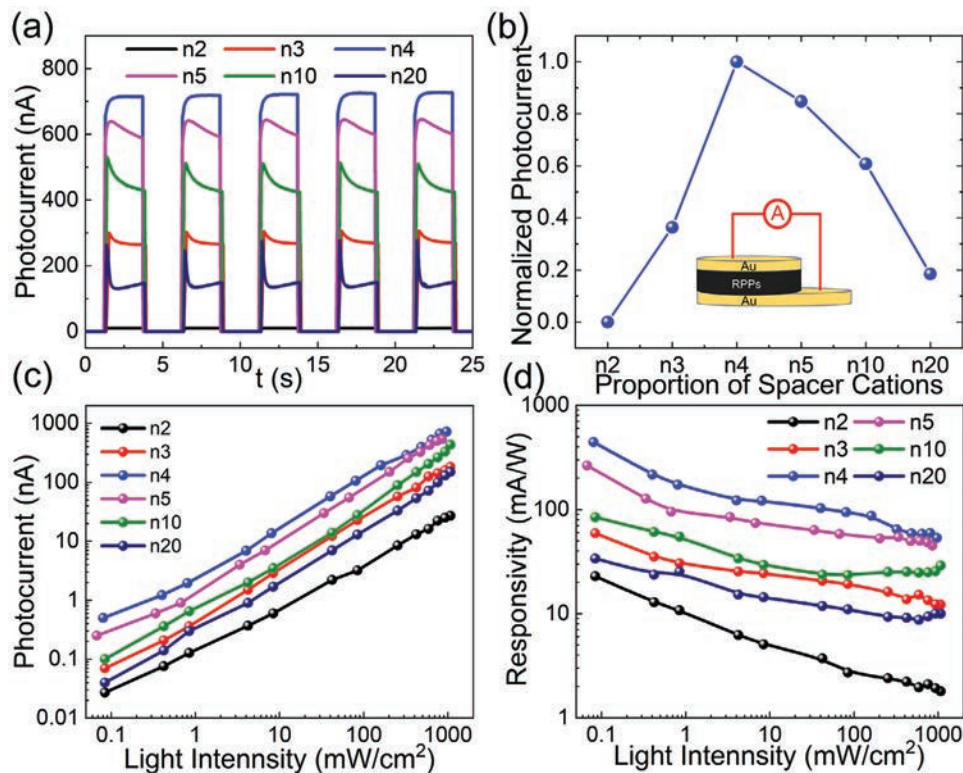


Figure 4. The performance of the self-powered photodetector based on the RPP films as the active layers, where the 450-nm laser is applied. a) Time-dependent photoresponse. b) Normalized photocurrent of the RPP films. c) Dependence of photocurrent on the light intensity. d) Dependence of responsivity on the light intensity.

all photocurrents under different light intensities are perfectly consistent with the results shown in Figure 4b. Accordingly, the corresponding responsivity and EQE values give the same trend as depicted in Figure 4d and Figure S13b, Supporting Information. However, the detectivity values of the samples with more *i*BA (i.e., *n*2 and *n*3) are superior to other ones except for *n*4, which can be attributed to the relatively low dark currents caused by a large amount of spacer cations (Figure S13a, Supporting Information).^[54] In this case, the performance of RPP based self-powered photodetectors is closely related to the proportion of spacer cations (*n* value) existed in the RPP films. In the future, to further enhance the performance parameters of these self-powered photodetectors, precisely controlling their amount of spacer cations is essential.

Furthermore, as mentioned above, the mechanical flexibility of RPP films is typically poor owing to the weak van der Waals interaction between their spacer layers. In this work, the flexibility study of the *n*4 based photodetector is focused. For a consistent comparison, both vertical-structure and conventional lateral-structure photodetectors utilizing the graded RPP phases are fabricated on flexible polyimide substrates, where the details can be found in the subsequent Experimental Section. At first, the influence of the bending radius on the photodetector performance is investigated, in which the measurement setup is depicted in the inset of Figure 5b,

demonstrating the accurate control of the bending radius. As shown in Figure 5a, there is not any degradation of the photocurrent of vertical-structure photodetector even after the device is bent down to a radius of 2 mm. However, the photocurrent of conventional lateral-structure photodetector decreases obviously as the bending radius decreases. Eventually, the photocurrent deteriorates to only 15% of its initial value when the bending radius comes to 4 mm. This significantly enhanced flexibility of the RPP based photodetector is anticipated to come from its unique vertical device structure. For the conventional lateral-structure photodetector, the weak van der Waals interaction between the spacer cations can easily be broken under tension during bending, which immensely hinders the propagation and collection of photo-carriers (Figure 5c). Interestingly, for the vertical-structure photodetector, as the carriers mainly transfer through the octahedral perovskite layers rather than the spacer cations with the larger resistance, the damage of van der Waals bonds among the spacer cations will hardly influence the photodetector performance (Figure 5d). The change of photocurrent is as well carefully investigated as the flexible photodetectors are bent to 9000 cycles with a fixed bending radius of 4 mm in each cycle, it is obvious that the superior mechanical flexibility of the vertical-structure device is confirmed again (Figure 5b). The photocurrent of lateral-structure photodetector distinctly

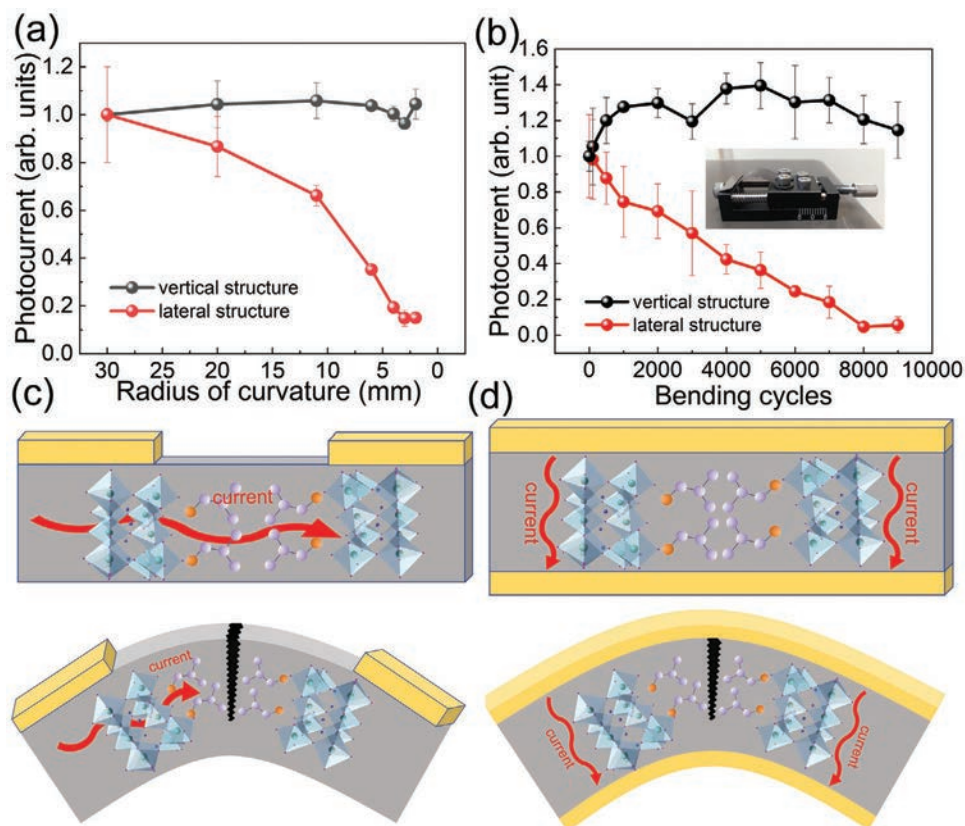


Figure 5. a) Dependence of the normalized photocurrent on the bending curvature of flexible vertical- and lateral-structure devices. b) Dependence of the normalized photocurrent on the bending cycles of all flexible devices. The inset shows the optical image of the measurement setup under the bending test. c,d) Schematic illustration of the current path within photodetectors with lateral and vertical structures before and after being bent.

decreases to only 4.6% of its initial value after it has been bent to 8000 cycles. However, for the vertical-structure counterpart, the photocurrent even increases slightly without any degradation as compared with its initial value. Through the optimal design of vertical device structure together with the graded RPP phases, the device flexibility is substantially enhanced, which surmount one of the main barriers that hinder its application for optoelectronic devices. **Table 1** summarizes the performances of quasi-2D perovskites based photodetectors in recent reports. Due to the self-assembly of graded RPP phases, the fabricated photodetector exhibits excellent device performance in self-powered characteristics, responsivity, response speed and mechanical flexibility.

3. Conclusion

In summary, high-performance flexible self-powered photodetectors based on graded RPP phases are fabricated in the vertical device structure. The self-assembly graded phase distribution in the order of n values configures a natural type-II band alignment along the out-of-plane direction of RPP films with spontaneous separation of photo-generated electrons and holes, which is utilized to construct the self-powered photodetectors for the first time. Without any driven voltage, the self-powered photodetectors exhibit an expressive responsivity of 444 mA W^{-1} and a fast response time of $52 \mu\text{s}$. When a driven voltage of 1.5 V is applied, the responsivity arrives at 3463 mA W^{-1} , while the response speed can be as fast as $24 \mu\text{s}$. More importantly, because of this vertical device structure, the mechanical flexibility of RPPs is greatly enhanced owing to the fact that the current prefers to flow through the metal halide octahedral layers between the top and bottom contact electrodes, being more tolerant to film damage. All these results would provide

Table 1. Comparison of various figure of merits of different 2D perovskites based photodetectors.

Perovskites	Bias [V]	Light	Flexible	R [mA W^{-1}]	Rise/decay time [ms]	Reference
$(\text{iBA})_2(\text{FA}_{0.60}\text{CS}_{0.10}\text{MA}_{0.40})_3\text{Pb}_4\text{I}_{13}$	1.5	532 nm	N	351	59/24	[42]
$(\text{BA})_2(\text{MA})\text{Pb}_2\text{I}_7$	40	N/A	N	21	53/19	[46]
2D FAPbI_3	9	645 nm	N	3270	0.35/0.54	[47]
$(\text{BPA})_2\text{PbBr}_4$	0	377 nm	N	0.1	0.027/0.03	[48]
$(\text{BA})_2(\text{MA})_2\text{Pb}_3\text{I}_{10}$	29.3	532 nm	N	12.78	10/7.5	[49]
$(\text{BA})_2(\text{MA})_{n-1}\text{Pb}_n\text{Br}_{3n+1}$ ($1 < n < \infty$) crystal	1	500 nm	N	190	210/240	[50]
$(\text{C}_4\text{H}_9\text{NH}_3)_2\text{PbBr}_4$ nanobelt	5	405 nm	Y	0.023	34/50	[51]
$(\text{PEA})_2\text{PbBr}_4$ single crystal	10	365 nm	N	31.48	0.41/0.37	[52]
BDAPbI_4 single crystal	10	462 nm	N	927	0.187/0.163	[53]
$(\text{iBA})_2(\text{MA})_3\text{Pb}_4\text{I}_{13}$ film	1.5	532 nm	N	117	16/15	[18]
$(\text{iBA})_2(\text{MA})_{n-1}\text{Pb}_n\text{I}_{3n+1}$ films	0	450 nm	Y	444	0.052/0.063	This work
	1.5	450 nm	Y	3463	0.024/0.025	

a promising and easy path to achieve high-performance self-powered photodetectors and at the same time to solve the issue of RPPs' poor flexibility, facilitating the further advancement of RPPs for optoelectronic devices.

4. Experimental Section

Synthesis of Perovskite Precursors: For the graded RPP films with different n values, different ratios of iBAI and MAI , and one mmol of PbI_2 at a molar ratio of $2:n-1:n$ were dissolved in 1 mL of dimethylformamide (DMF). The solutions were then stirred at room temperature overnight.

Device Fabrication: The perovskite films were fabricated by a one-step spin-coating method in a nitrogen-filled glovebox, where the oxygen and moisture concentration were well controlled at the ppm level. The glass and PI substrates were first ultrasonically washed by acetone, ethanol, and deionized (DI) water for 15 min in succession. After that, a 50-nm-thick Au film was thermally evaporated onto the substrates. Then, these substrates were treated with a mild oxygen plasma for 10 min (0.26 Torr, 30 W). For the fabrication of RPP films, 40 μL of precursor solution was spin-coated on the glass/Au or PI/Au substrate at 3000 rpm for 30 s, followed with thermal annealing at $100 \text{ }^\circ\text{C}$ for 10 min for the full crystallization of samples. Finally, with the assistance of a shadow mask, another 50-nm-thick Au electrodes with a diameter of 70 μm were thermally evaporated onto the films.

Film and Device Characterization: Surface morphologies of the RPP films with different n values were characterized with scanning electron microscopy (SEM, FEI Quanta 450 FEG SEM) and atomic force microscopy (AFM, Bruker Dimension Icon AFM). X-ray diffraction (XRD, D2 Phaser with $\text{Cu K}\alpha$ radiation, Bruker) was used to evaluate the crystallinity and crystal structure of the obtained films. UV-vis absorption spectra and the optical transmission of prepared Au films were recorded using a PerkinElmer model Lambda 2S UV-vis spectrometer. The PL spectra were acquired by a Hitachi F-4600 spectrophotometer with an excitation wavelength of 470 nm. The electrical performance of fabricated devices was characterized by a standard electrical probe station and an Agilent 4155C semiconductor analyzer (Agilent Technologies, California, USA). A 532 nm laser diode was used as a light source for the photodetector measurement, while the power of the incident irradiation was measured using a power meter (PM400, Thorlabs). An attenuator was also employed to tune the irradiation power illuminating on the device. For determining the response time of the detector, a low-noise current amplifier (SR570, Stanford Research Systems, USA) combined with a digital oscillator (TBS 1102B EDU, Tektronix, USA) was used to obtain high-resolution current-time curves. The schematic of the measurement system is demonstrated in Figure S14, Supporting Information.

Supporting Information

Supporting Information is available from the Wiley Online Library or from the author.

Acknowledgements

The authors acknowledge the General Research Fund (CityU 11204618) and the Theme based Research (T42-103/16-N) of the Research Grants Council of Hong Kong SAR, China, and the Foshan Innovative and Entrepreneurial Research Team Program (No. 2018IT100031).

Conflict of Interest

The authors declare no conflict of interest.

Data Availability Statement

The data that support the findings of this study are available from the corresponding author upon reasonable request.

Keywords

Flexible, halide perovskites, photodetectors, quasi-2D, self-powered

Received: January 24, 2021

Revised: February 21, 2021

Published online: April 23, 2021

- [1] F. P. García de Arquer, A. Armin, P. Meredith, E. H. Sargent, *Nat. Rev. Mater.* **2017**, 2, 16100.
- [2] X. Gong, M. Tong, Y. Xia, W. Cai, J. S. Moon, Y. Cao, G. Yu, C. L. Shieh, B. Nilsson, A. J. Heeger, *Science* **2009**, 325, 1665.
- [3] H. Wang, D. H. Kim, *Chem. Soc. Rev.* **2017**, 46, 5204.
- [4] L. Zhao, K. Roh, S. Kacmoli, K. Al Kurdi, S. Jhulki, S. Barlow, S. R. Marder, C. Gmachl, B. P. Rand, *Adv. Mater.* **2020**, 32, 2000752.
- [5] L. Wang, Y. Xue, M. Cui, Y. Huang, H. Xu, C. Qin, J. Yang, H. Dai, M. Yuan, *Angew. Chem., Int. Ed.* **2020**, 59, 6442.
- [6] W. Ke, I. Spanopoulos, Q. Tu, I. Hadar, X. Li, G. S. Shekhawat, V. P. Dravid, M. G. Kanatzidis, *J. Am. Chem. Soc.* **2019**, 21, 8627.
- [7] S. Bai, P. Da, C. Li, Z. Wang, Z. Yuan, F. Fu, M. Kawecki, X. Liu, N. Sakai, J. T. Wang, S. Huettner, S. Buecheler, M. Fahlman, F. Gao, H. J. Snaith, *Nature* **2019**, 571, 245.
- [8] R. Saraf, V. Maheshwari, *ACS Appl. Mater. Interfaces* **2018**, 10, 21066.
- [9] N. Wei, Y. Chen, Y. Miao, T. Zhang, X. Wang, H. Wei, Y. Zhao, *J. Phys. Chem. Lett.* **2020**, 11, 8170.
- [10] L. McGovern, M. H. Futscher, L. A. Muscarella, B. Ehrler, *J. Phys. Chem. Lett.* **2020**, 11, 7127.
- [11] G. Gordillo, O. G. Torres, M. Camila, J. C. Peña, O. Virguez, *J. Mater. Res. Technol.* **2020**, 9, 13759.
- [12] H. Ren, S. Yu, L. Chao, Y. Xia, Y. Sun, S. Zuo, F. Li, T. Niu, Y. Yang, H. Ju, B. Li, H. Du, X. Gao, J. Zhang, J. Wang, L. Zhang, Y. Chen, W. Huang, *Nat. Photonics* **2020**, 14, 154.
- [13] J. Qiu, Y. Xia, Y. Zheng, W. Hui, H. Gu, W. Yuan, H. Yu, L. Chao, T. Niu, Y. Yang, X. Gao, Y. Chen, W. Huang, *ACS Energy Lett.* **2019**, 4, 1513.
- [14] J. Qiu, Y. Zheng, Y. Xia, L. Chao, Y. Chen, W. Huang, *Adv. Funct. Mater.* **2019**, 29, 1806831.
- [15] Y. Chen, Y. Sun, J. Peng, J. Tang, K. Zheng, Z. Liang, *Adv. Mater.* **2018**, 30, 1703487.
- [16] C. R. Kagan, D. B. Mitzi, C. D. Dimitrakopoulos, *Science* **1999**, 286, 945.
- [17] C. C. Stoumpos, D. H. Cao, D. J. Clark, J. Young, J. M. Rondinelli, J. I. Jang, J. T. Hupp, M. G. Kanatzidis, *Chem. Mater.* **2016**, 28, 2852.
- [18] R. Dong, C. Lan, X. Xu, X. Liang, X. Hu, D. Li, Z. Zhou, L. Shu, S. Yip, C. Li, S. Tsang, J. C. Ho, *ACS Appl. Mater. Interfaces* **2018**, 10, 19019.
- [19] Z. Lai, R. Dong, Q. Zhu, Y. Meng, F. Wang, F. Li, X. Bu, X. Kang, H. Zhang, Q. Quan, W. Wang, F. Wang, S. Yip, J. C. Ho, *ACS Appl. Mater. Interfaces* **2020**, 12, 39567.
- [20] Z. Xu, M. Chen, S. F. Liu, *J. Phys. Chem. Lett.* **2019**, 10, 3670.
- [21] S. T. Ha, X. Liu, Q. Zhang, D. Giovanni, T. C. Sum, Q. Xiong, *Adv. Opt. Mater.* **2014**, 2, 838.
- [22] S. Niu, X. Wang, F. Yi, Y. S. Zhou, Z. L. Wang, *Nat. Commun.* **2015**, 6, 8975.
- [23] J. Chen, Y. Huang, N. Zhang, H. Zou, R. Liu, C. Tao, X. Fan, Z. L. Wang, *Nat. Energy* **2016**, 1, 16138.
- [24] H. Zhou, Z. Song, C. R. Grice, C. Chen, J. Zhang, Y. Zhu, *Nano Energy* **2018**, 53, 880.
- [25] F. Cao, W. Tian, K. Deng, M. Wang, L. Li, *Adv. Funct. Mater.* **2019**, 29, 1906756.
- [26] V. Pecunia, Y. Yuan, J. Zhao, K. Xia, Y. Wang, S. Duhm, L. Portilla, F. Li, *Nano-Micro Lett.* **2020**, 1, 27.
- [27] J. Yang, B. D. Siempelkamp, E. Mosconi, F. De Angelis, T. L. Kelly, *Chem. Mater.* **2015**, 27, 4229.
- [28] Z. Zhang, W. Zhang, Q. Jiang, Z. Wei, M. Deng, D. Chen, W. Zhu, J. Zhang, H. You, *ACS Appl. Mater. Interfaces* **2020**, 12, 6607.
- [29] Q. Jiang, X. Zhang, J. You, *Small* **2018**, 14, 1801154.
- [30] H. N. Chen, Z. H. Wei, H. X. He, X. L. Zheng, K. S. Wong, S. H. Yang, *Adv. Energy Mater.* **2016**, 6, 1502087.
- [31] W. Zhu, Q. Zhang, D. Chen, Z. Zhang, Z. Lin, J. Chang, J. Zhang, C. Zhang, Y. Hao, *Adv. Energy Mater.* **2018**, 8, 1802080.
- [32] J. Liu, J. Leng, K. Wu, J. Zhang, S. Jin, *J. Am. Chem. Soc.* **2017**, 139, 1432.
- [33] J. Jiang, X. Zou, Y. Lv, Y. Liu, W. Xu, Q. Tao, Y. Chai, L. Liao, *Nat. Commun.* **2020**, 11, 4266.
- [34] J. M. Hoffman, J. Strzalka, N. C. Flanders, I. Hadar, S. A. Cuthriell, Q. Zhang, R. D. Schaller, W. R. Dichtel, L. X. Chen, M. G. Kanatzidis, *Adv. Mater.* **2020**, 32, 2002812.
- [35] J. Hu, I. W. H. Oswald, S. J. Stuard, M. M. Nahid, N. Zhou, O. F. Williams, Z. Guo, L. Yan, H. Hu, Z. Chen, X. Xiao, Y. Lin, Z. Yang, J. Huang, A. M. Moran, H. Ade, J. R. Neilson, W. You, *Nat. Commun.* **2019**, 10, 1276.
- [36] R. Quintero-bermudez, A. H. Proppe, A. Mahata, P. Todorovic, S. O. Kelley, F. De Angelis, E. H. Sargent, *J. Am. Chem. Soc.* **2019**, 141, 13459.
- [37] X. Zhang, R. Munir, Z. Xu, Y. Liu, H. Tsai, W. Nie, J. Li, T. Niu, D. Smilgies, M. G. Kanatzidis, A. D. Mohite, K. Zhao, A. Amassian, S. F. Liu, *Adv. Mater.* **2018**, 30, 1707166.
- [38] M. Li, Q. Gao, P. Liu, Q. Liao, H. Zhang, J. Yao, W. Hu, Y. Wu, H. Fu, *Adv. Funct. Mater.* **2018**, 28, 1707006.
- [39] O. Lopez-Sanchez, D. Lembke, M. Kayci, A. Radenovic, A. Kis, *Nat. Nanotechnol.* **2013**, 8, 497.
- [40] F. Binet, J. Y. Duboz, E. Rosencher, F. Scholz, V. Härle, *Appl. Phys. Lett.* **1996**, 69, 1202.
- [41] C. Soci, A. Zhang, B. Xiang, S. A. Dayeh, D. P. R. Aplin, J. Park, X. Y. Bao, Y. H. Lo, D. Wang, *Nano Lett.* **2007**, 7, 1003.
- [42] R. Dong, C. Lan, F. Li, S. P. Yip, J. C. Ho, *Nanoscale Horiz.* **2019**, 4, 1342.
- [43] X. W. Tong, W. Y. Kong, Y. Y. Wang, J. M. Zhu, L. B. Luo, Z. H. Wang, *ACS Appl. Mater. Interfaces* **2017**, 9, 18977.
- [44] Y. Meng, C. Lan, F. Li, S. Yip, R. Wei, X. Kang, X. Bu, R. Dong, H. Zhang, J. C. Ho, *ACS Nano* **2019**, 13, 6060.
- [45] H. P. Wang, S. Li, X. Liu, Z. Shi, X. Fang, J. H. He, *Adv. Mater.* **2021**, 33, 2003309.
- [46] M. Min, R. F. Hossain, L.-C. Ma, A. B. Kaul, *J. Vac. Sci. Technol. A* **2020**, 38, 052202.
- [47] D. Yu, F. Cao, Y. Gu, Z. Han, J. Liu, B. Huang, X. Xu, H. Zeng, *Nano Res.* **2021**, 14, 1210.
- [48] C. Ji, D. Dey, Y. Peng, X. Liu, L. Li, J. Luo, *Angew. Chemie – Int. Ed.* **2020**, 59, 18933.
- [49] J. Zhou, Y. Chu, J. Huang, *ACS Appl. Mater. Interfaces* **2016**, 8, 25660.
- [50] J. Chen, Y. Wang, L. Gan, Y. He, H. Li, T. Zhai, *Angew. Chemie – Int. Ed.* **2017**, 56, 14893.
- [51] B. S. Zhu, Z. He, J. S. Yao, C. Chen, K. H. Wang, H. Bin Yao, J. W. Liu, S. H. Yu, *Adv. Opt. Mater.* **2018**, 6, 1701029.
- [52] Y. Zhang, Y. Liu, Z. Xu, H. Ye, Q. Li, M. Hu, Z. Yang, S. Liu, *J. Mater. Chem. C* **2019**, 7, 1584.
- [53] Y. Zhang, Y. Liu, Z. Xu, Z. Yang, S. Liu, *Small* **2020**, 16, 2003145.
- [54] J. Hu, L. Yan, W. You, *Adv. Mater.* **2018**, 30, 1802041.